ChemElectroChem

Research Article
doi.org/10.1002/celc.202201118

Chemistry Europe
European Chemical Societies Publishing

www.chemelectrochem.org

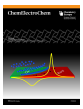

A Thermodynamic Model for the Insertion Electrochemistry of Battery Cathodes

Keyvan Malaie,* Fritz Scholz, and Uwe Schröder*[a]

The authors dedicate this paper to the memory of Alexander Milchev (1943–2022), a pioneer of nucleation/growth science and a researcher with highest human qualities

The transition to Ni-based battery cathodes enhances the energy density and reduces the cost of batteries. However, this comes at the expense of losing energy efficiency which could be a consequence of charge–discharge hysteresis. Here, a thermodynamic model is developed to understand the extent and origin of charge–discharge hysteresis in battery cathodes based on their cyclic voltammograms (CVs). This was possible by defining a Gibbs energy function that weights random ion insertion/expulsion, i.e., a solid solution pathway, against selective ion insertion/expulsion, i.e., a phase separation route. The model was verified experimentally by the CVs of CoOOH and $Ni(OH)_2$ as solid-solution and phase-separating cathodes, respectively. Finally, a microscopic view reveals that phase separation and hysteresis are a consequence of large ionic radii difference of the reduced and oxidized central metal atoms.

Introduction

Ion-insertion batteries are probably the most efficient and clean energy packages at present that are preferred by automobile industries. Li-ion batteries based on $LiCoO_2$ or $LiNi_xCo_yMn_yO_2$ (NMC, 1:1:1) cathodes have been trend-setting for the last three decades. However, Ni-rich cathodes offer a higher energy density and the natural abundance of nickel is higher, but they suffer from poor structural performance stability and energy efficiency.[1,2] At a macroscopic level, this problem manifests in energy losses during a charging-discharging cycle. This phenomenon could be a consequence of charge–discharge hysteresis which is an inherent feature of not only Ni-based cathodes,[3–5] but also many other battery materials[6–8] including the prototypical $LiFe_2O_4$.[9,10] Charge–discharge hysteresis in batteries has recently attracted an increasing attention but is yet poorly understood, because contrary to soluble redox species, the electrochemical thermodynamic and kinetics of solid redox systems have not been developed as much.[11–13]

The majority of the present models for solid redox systems are based on kinetics that have a serious difficulty. The strongly-interacting solid redox species make any governing differential equation non-linear, in contrast to soluble species that can be described with the linear equations of Fick's law[14] or the Butler-Volmer equation. In addition, contrary to the semi-infinite diffusion assumed for soluble species, the initial condition is not well-defined in the solid phase. For instance, recently Doménech-Carbó has approximated the nonlinear behavior of solid redox species with a logistic equation – though warranted only for discrete phenomena – but without defining the initial condition.[15] A similar problem also exists for the cumbersome kinetic equations recently proposed for solid redox monolayers.[16–19]

Laviron was probably the first to use a thermodynamic model to describe the voltammetry of interacting adsorbed species based on the Frumkin isotherm,[20,21] which later was further employed to describe the intercalation electrochemistry of lithium-ion batteries.[22,23] These models that are based on adsorption isotherms or solid-solution treatment of redox species[24] give trivial information about the insertion electrochemistry and the phase transitions, missing a microscopic insight or physical explanation for the underlying interactions. In fact, since ion-insertion models are generally based on the knowledge of surface adsorption, "interaction" is treated as if it occurs among the insertion ions in the solid. As of today, there is no thermodynamic model to understand the cyclic voltammetry data of solid redox species such as those of battery materials, and the underlying interactions and the charge–discharge hysteresis in battery systems remain an anomaly.

Here, we present a thermodynamic model to understand the voltammetric data of battery cathodes, e.g., CoOOH and $Ni(OH)_2$. This model is based on the interactions among the solid redox species and captures the CV features such as the Full Width at Half Maximum (FWHM) and peak separation. It reveals that charge–discharge hysteresis is a consequence of phase separation, i.e., of an interfacial tension energy. Furthermore, a microscopic view of the materials reveals that phase separation results from the radius change of central metal ions during charge–discharge. For experimental simplicity, the model is verified in aqueous solution, but it is also applicable to non-aqueous systems, i.e., Li-ion battery, because the model is

[a] K. Malaie, F. Scholz, U. Schröder
Institute of Biochemistry
University of Greifswald
Felix-Hausdorff-Str. 4, 17487 Greifswald (Germany)
E-mail: keyvan.malaie@uni-greifswald.de
uwe.schroeder@uni-greifswald.de

Supporting information for this article is available on the WWW under https://doi.org/10.1002/celc.202201118

completely based on solid phase features (e.g., crystal lattice) and does not consider liquid solution or interface features such as ion diffusion and impedance.

Results and Discussion

Macroscopic View

In an aqueous environment, protons from the aqueous solution are considered as the ions that are inserted and expelled in the course of electrochemical reactions of the two cathode materials (Eqs. 1–3):

$$CoO_2\ (s) + H^+\ (aq) + e^- \leftrightarrows CoOOH\ (s) \tag{1}$$

$$NiOOH\ (s) + H^+\ (aq) + e^- \leftrightarrows Ni(OH)_2\ (s) \tag{2}$$

Or generally:

$$Ox\ (s) + H^+\ (aq) + e^- \leftrightarrows Red\ (s) \tag{3}$$

For the latter equation, the Nernst equation can be expressed as follows (Eqs. 4–6):

$$E^1 = E^0 + \frac{RT}{F}\ln\frac{a_{Ox}a_{H^+}}{a_{Red}} \tag{4}$$

$$E^1 = E^0 + \frac{RT}{F}\ln\frac{\gamma_{Ox}\gamma_{H^+}}{\gamma_{Red}} + \frac{RT}{F}\ln\frac{C_{Ox}C_{H^+}}{C_{Red}} \tag{5}$$

$$E^1 = E^{0'} + \frac{RT}{F}\ln\frac{C_{Ox}C_{H^+}}{C_{Red}} \tag{6}$$

E^0 and γ denote the standard potential of the redox couple and the activity coefficient. $E^{0'}$ is the formal potential that incorporates activity coefficients, and other symbols have their usual meaning. Since C_{H^+} is the concentration of proton in the electrolyte, and hence constant, we can define a new potential that only depends on the concentrations of the redox couple (Eq. 7). Thus, by re-arranging Eq. 6:

$$E = E^1 - \frac{RT}{F}\ln C_{H^+} = E^{0'} + \frac{RT}{F}\ln\frac{C_{Ox}}{C_{Red}} \tag{7}$$

Since in a closed system we have $C_{ox}+C_{red}=C_{total}$ or $x_{ox}+x_{red}=1$ based on mole ratios, Eq. 7 can be written as a function of x_{red} only, or in simple notation x, as follows (Eq. 8):

$$E = E^{0'} + \frac{RT}{F}\ln\frac{1-x}{x} \tag{8}$$

In other terminology that is used for lithium-ion batteries, x is equivalent to the deintercalation level or fraction. Additionally, Eq. 8 inherently assumes that there is no interaction among the redox species, i.e., random ion (de)insertion, that is normally the case of dilute soluble redox species.

In the next section, the mixing of Ox and Red species in this redox system (Eq. 3) is considered.

Homogeneous System

The mixing entropy (ΔS_{mix}) of a homogeneous system consisting of Ox and Red species with no particle interaction, i.e., behaving like an ideal gas, is equal to:

$$\Delta S_{mix} = k_B \ln W \tag{9}$$

Where k_B and W are Boltzmann constant and the number of microstates, respectively. W can be determined by evaluating the total number of distinguishable permutations of Ox and Red entities as follows:

$$W = \frac{N!}{N_{Ox}!N_{Red}!} \tag{10}$$

In which N_{Ox}, N_{Red}, and N are the number of OX and Red entities and their sum, respectively. Since these are very large numbers, their factorials can be estimated according to the Sterling's approximation (See Sec. 1.1, ESI). Hence:

$$\Delta S_{mix} = -k_B\left[N_{Ox}\ln\frac{N_{Ox}}{N} + N_{Red}\ln\frac{N_{Red}}{N}\right] \tag{11}$$

Eq. 11 can be alternatively expressed in mole ratios as follows:

$$\Delta S_{mix} = -k_B N[x_{Ox}\ln x_{Ox} + x_{Red}\ln x_{Red}] \tag{12}$$

Since $k_B = R/N_a$, where N_a is the Avogadro constant, $n = N/N_a$ is the number of moles, and $x_{ox}+x_{red}=1$, eq. 12 can be expressed as a function of x_{red} only or simply x:

$$\Delta S_{mix} = -nR[x\ln x + (1-x)\ln(1-x)] \tag{13}$$

Finally, we remind that the Gibbs energy of mixing (ΔG_{mix}) is equal to $\Delta H_{mix} - T\Delta S_{mix}$, in which the enthalpy of mixing (ΔH_{mix}) is zero for a non-interacting system. Hence, ΔG_{mix} can simply be obtained from eq. 13:

$$\Delta G_{mix} = RT[x\ln x + (1-x)\ln(1-x)] \tag{14}$$

ΔG_{mix} is the molar Gibbs energy of mixing in a homogeneous system, and from here on it is shown simply as ΔG_h. When the two components interact with each other, the Gibbs energy includes also an enthalpy term equal to $Ax(1-x)$ with A ($J\,mol^{-1}$) being the proportionality constant. A can be converted to a dimensionless parameter by setting $A = gRT/2$, where g is an interaction parameter having values $0 \le g < 4$ with the higher g values indicating stronger repulsive/attractive interactions. Adding this enthalpy term to Eq. (14):

$$\Delta G_h = RT\left[x\ln x + (1-x)\ln(1-x) + \frac{g}{2}x(1-x)\right] \quad (15)$$

ΔG_h can be differentiated with respect to x to get the chemical potential (μ):

$$\mu = \frac{d\Delta G_h}{dx} = RT\left[\ln\left(\frac{x}{1-x}\right) + \frac{g}{2}(1-2x)\right] \quad (16)$$

If we set up an electrochemical cell to measure μ, we have $\mu = -F(E-E^{0'})$ for a one-electron transfer reaction, with F and $E^{0'}$ denoting the Faraday constant and the formal potential vs. the reference electrode. Hence, substituting for μ in Eq. 16:

$$E - E^{0'} = \frac{RT}{F}\left[\ln\left(\frac{1-x}{x}\right) + \frac{g}{2}(2x-1)\right] \quad (17)$$

Eq. 17 maybe compared with the Nernst equation modified by the one-parameter activity model, i.e., the Margules expression.[25] Furthermore, Eq. 17 reduces to the Nernst equation (Eq. 8) for $g = 0$.

Next, we extract the electric current from Eq. 17. First, the chain rule is applied to the differential definition of electric current as follows:

$$i = \frac{dq(t)}{dt} = \frac{dq(t)}{dE}\frac{dE}{dt} \quad (18)$$

In which the first and second term are differential capacitance (C_{dif}) and potential scan rate (ν), respectively. We remind that by using the Faraday rule the mole ratio can alternatively be expressed as $x = q(t)/q_1$ with q_1 denoting the total charge. Hence, $q(t)$ in Eq. 18 is substituted with $q_1 x$ as follows:

$$i = q_1 \nu \frac{dx}{dE} \quad (19)$$

Now, by evaluating dx/dE from Eq. 17 and substituting it in Eq. 19, the current is obtained as follows:

$$i = \frac{Fq_1\nu}{RT}\left[\frac{x(1-x)}{gx(1-x)-1}\right] \quad (20)$$

Eq. 20 in combination with Eq. 17 describe the $i-E$ curves, or CV, of a homogeneous solid redox system under various interparticle interactions (g).

Heterogeneous system

The interaction parameter g can be expressed in terms of three types of interactions that exist in a two-component system: $g = a_{RedRed} + a_{OxOx} - 2a_{OxRed}$ with a_{RedRed}, a_{OxOx}, and a_{OxRed} signifying Red–Red, Ox–Ox, and Ox–Red interactions. Thus, when $g = 0$ either there are no interactions (i.e., behaving like an ideal gas) or the interactions are balanced. When $g > 0$ the attractive interactions among identical species, i.e., Red-Red or Ox–Ox, are stronger, favoring phase separation (e.g., sparingly-soluble salt). For these later particles to dissolve in each other to any extent, that is to form a solid solution during charge/discharge, they have to overcome an interfacial energy (ΔG_i) between the two phases in addition to the homogeneous Gibbs energy. Thus:

$$\Delta G_t = \Delta G_h + \Delta G_i \quad (21)$$

ΔG_t is the Gibbs energy of the heterogeneous system. We propose that ΔG_i has the following form:

$$\Delta G_i = RT\gamma e^{\alpha x} \quad (22)$$

in which γ is the interfacial tension parameter that scales with g (e.g., $\gamma = 2g$) and α is a symmetry factor between forward and backward reaction with α for forward and $(0.5-\alpha)$ for backward reaction (See Sec. 1.2, ESI). Contrary to a random ion insertion/expulsion, if by going from Ox state to the Red state an Ox–Red interface is created, the same interface cannot be re-established in the backward direction. In other words, the higher the interfacial energy of going from Ox to Red, the lower it can be in the backward direction (Scheme 1). $\alpha = 0.25$ and 0 correspond to completely symmetric and dissymmetric modes of reaction, respectively.

Repeating the same process as in the previous discussion gives the potential and current of the heterogeneous system. The potential and current function for the forward reaction are as follows:

$$f(E-E^0) = \ln\left(\frac{1-x}{x}\right) - \frac{\gamma}{4}(1-2x) - \gamma\alpha e^{\alpha x} \quad (23)$$

$$i_f = \frac{fq_1\nu x(1-x)}{\gamma(0.5-\alpha^2 e^{\alpha x})x(1-x)-1} \quad (24)$$

in which $f = F/RT$ is used. Similarly, for the backward reaction, by substituting α with $0.5-\alpha$ in Eq. 23 and repeating the same process for obtaining the backward current (i_b):

$$i_b = \frac{fq_1\nu x(1-x)}{\gamma[0.5-(0.5-\alpha)^2 e^{(0.5-\alpha)x}]x(1-x)-1} \quad (25)$$

The first term on the right-hand side of Eq. 23 represents random ion insertion/expulsion and the other two terms represent non-random ion insertion/expulsion. i_f in Eq. 24 denotes the forward current and has the same form as that of homogeneous equation (Eq. 20) except that g is not a constant anymore. Both homogeneous and heterogeneous current equations show a linear dependence of current (i) on scan rate (ν), signifying a pseudocapacitive feature rather than a diffusion-limited process.

Figure 1a illustrates simulated CV curves plotted based on the homogeneous model for different g values. This simulation predicts that under no inter-particle interaction ($g = 0$), i.e.,

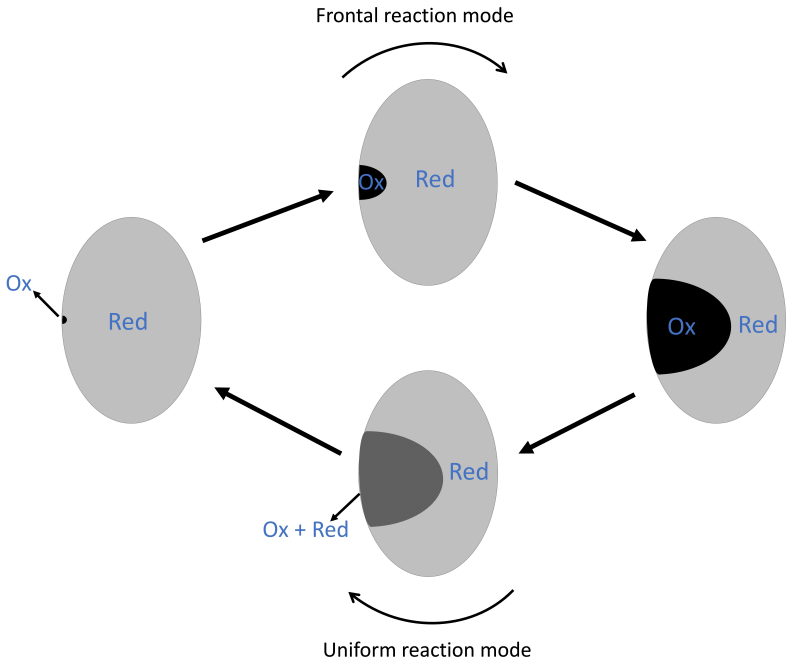

Scheme 1. An illustration of the electrode surface during oxidation accompanied with ion deinsertion (forward arrows) and reduction accompanied with ion insertion (backward arrows) displaying a hysteresis loop due to different (de)insertion reaction modes, namely, frontal reaction (or deinsertion wave) and uniform insertion reaction, respectively. The OX and Red denote oxidized and reduced particles. This reaction dissemetry is parametrized with α in Eq. 22.

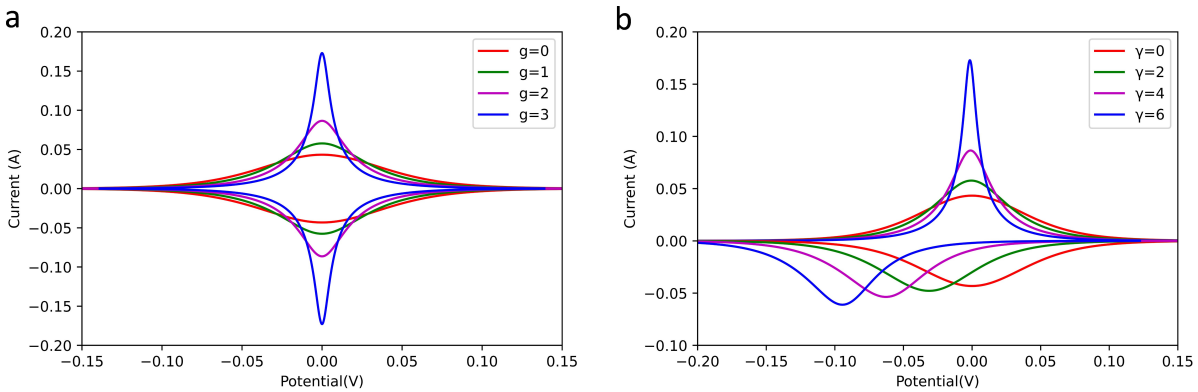

Figure 1. Modelled CV curves of solid redox systems. a) a hemogeneous system with different interaction parameters based on equations 17 and 20, and b) a heterogeneous system with different interfacial tension parameters based on Eq. 23 and 24 for the backward current and Eq. 23 which α substituted by $0.5-\alpha$ and Eq. 25 for the forward current ($\nu = 5$ mV s^{-1}, $q = 1\times10^{-5}$, $T = 298$, and $\alpha = 0.01$). The potnetial axis represents $E - E^{0\prime}$ that is the overpotential.

random ion insertion/expulsion, the CV curves obey the Nernstian behavior for which the full width at half maximum (FWHM) is 90.6 mV (See Sec. 1.3, ESI), and as g increases the FWHM decreases. These CV curves are similar to the voltammetric peaks that Conway obtained for redox monolayers (adsorption pseudocapacitor) by assuming a Frumkin adsorption isotherm, and he further stated that a pseudocapacitive ion-inserting compound would have the same voltammetric peak.[26] Nevertheless, these narrow and symmetric CV peaks for $g \neq 0$ are rarely observed experimentally for ion-inserting compounds, because as shown above they correspond to an ideal gas model and not a solid redox phase.

Figure 1b exhibits the CV curves plotted based on the equations of the heterogeneous model (Eq. 23 and 24 for the backward branch, and Eq. 23 with α substituted by $0.5-\alpha$ and Eq. 25 for the forward branch) for different γ values. Again $\gamma = 0$ corresponds to the Nernstian system, but as γ increases it creates two effects: 1) disproportioning the FWHMs for the oxidation and reduction reactions and 2) hysteresis in the peak potentials. The effect of α parameter is to create peak potential hysteresis without changing the mid-peak potential (Figure S1, ESI).

The homogeneous and the heterogeneous model were used to analyze the cyclic voltammetry of CoOOH and $Ni(OH)_2$ electrodes. Figure 2a and b exhibit the CV peak currents of these electrodes at scan rates, ν, between 1 to 200 mV s^{-1} in 0.1 M KOH. Both electrodes exhibit a linear relationship between i_p and ν, revealed by a slope of nearly unity for the respective

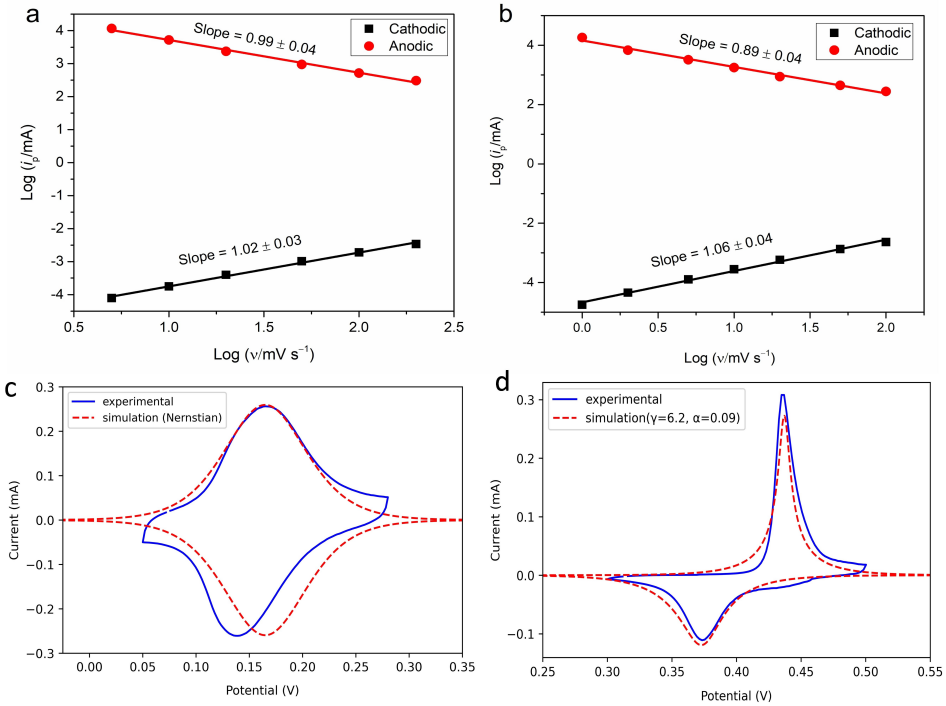

Figure 2. The effect of potential scan rate on the CV peak currents for CoOOH (a) and $Ni(OH)_2$ electrodes in 0.1 M KOH (pH = 12.8). CV curves of CoOOH (c) and $Ni(OH)_2$ (d) at the scan rates of 10 and 5 mV s^{-1} respectitvely in 0.1 M KOH (pH = 12.8).

log(i_p)–log(ν) curves. Thus, the application of the CV models to these systems is warranted. Figure 2c displays an overlay of the experimental CV of CoOOH and that of the homogeneous model for the scan rate of 10 mV s^{-1}. The oxidation peak almost completely overlaps with that from the model with FWHM = 90 mV, verifying a one-electron transfer reaction with nearly random ion insertion/expulsion (Nernstian) behavior. During reduction, however, a peak hysteresis of about 25 mV is observed with $g = 0.2$ and FWHM < 90 mV, indicating a non-ideal random ion insertion behavior.

Figure 2d illustrates the CV curve of $Ni(OH)_2$ obtained from experiment and the heterogeneous model with $\gamma = 6.2$ and $\alpha = 0.09$ at 5 mV s^{-1}. The high value of γ and a low value of α indicate a strong dissymmetry in the ion (de)insertion reaction modes. The FWHM is about 18 mV for oxidation indicating a selective ion deinsertion, i.e., frontal reaction mode, but it is about 30 mV for reduction indicating a smaller contribution of the frontal reaction mode.

Microscopic View

During electrodeposition of CoOOH and $Ni(OH)_2$, both films crystalize in a layered structure intercalated with water molecules, i.e., in an α phase,[27,28] and both electrodes undergo a one-electron transfer proton insertion/expulsion reaction. Furthermore, Co and Ni atoms are located just next to each other in the periodic table. Nonetheless, as shown above, $Ni(OH)_2$ goes through a phase separation but CoOOH exhibits almost an ideal series of solid solutions. This can be explained by looking at the electronic configurations of the central ions in the octahedral field of oxygens for these crystals before and after oxidation (Scheme S1). In case of CoOOH ($t_{2g}^4 e_g^2$) the electron is removed from a non-axial orbital (t_{2g}^4) with minimal effect on the p–d electronic repulsion and polyhedral distortion, but for $Ni(OH)_2$ ($t_{2g}^6 e_g^2$) the electron is removed from an axial orbital (e_g^2)[29] that significantly reduces the repulsion between $d_{x^2-y^2}$ of nickel and the p_x of oxygen, causing a lattice cell contraction. Kondrakov et al. have made similar observations for Li-insertion in Ni-rich cathodes by X-ray diffraction measurements.[30,31]

More specifically, removing an electron from the $d_{x^2-y^2}$ orbital of Ni creates a Jahn–Teller distortion effect by contracting the *xy* plane and elongating the *z* axis bonds in order to stabilize NiOOH ($t_{2g}^6 e_g^1$) (polyhedral distortion is defined as the variance of metal-oxygen bond lengths vs. mean bond length[32]).

Here, we introduce a change in the ionic radii of the central metal ions during oxidation (Δr) as a descriptor for phase separation, i.e., $\gamma = f(\Delta r)$, assuming that the compounds undergo a well-defined one-electron transfer reaction accompanied by one proton transfer, and that a reliable determination of ionic radii is available. The determination of ionic radii (*r*) is clearly influenced by coordination number (CN),[32] apart from the oxidation state, electronic configuration, and a possible polyhedral distortion mentioned above. In case of $Ni(OH)_2$ and CoOOH, the layered structure and octahedral configuration (CN = 6) are retained after oxidation, but the interlayer protons change from 2 to 1 and 1 to 0 per metal atom,

respectively.[29,33–35] Furthermore, the most stable electronic configurations of their d orbitals (low spin vs. high spin) should be considered.[36] Table 1 lists the ionic radii (r) and ionic radii difference (Δr) of Co and Ni central ions with octahedral coordination considering an average polyhedral distortion before and after oxidation.[32]

The difference in the Δr of the two redox couples has the following consequence for the electrochemical ion-(de)insertion reaction. CoOOH with $\Delta r = 0.01$ Å shows nearly a random oxidation of the atoms, i.e., random expulsion of the protons (Scheme 2a), but for $Ni(OH)_2$ with $\Delta r = 0.13$ Å, the oxidation of first few atoms creates an interfacial tension (Scheme 2b); it destabilizes the next Ni^{2+} octahedrons due to the significant contraction of the oxidized Ni^{3+} octahedrons, thus making the frontal reaction mode preferable over the uniform reaction mode. Because of this significant cell contraction, the removal of first few electrons from the $Ni(OH)_2$ electrode is difficult which delays the onset oxidation potential (Figure 2d), but once initiated it proceeds over a narrow potential range because of the unstable juxtaposed Ni^{2+} octahedrons. Other cathode materials from the literature also agree with this microscopic view. For example, $LiFePO_4$, a well-known cathode that undergoes phase separation during charge–discharge, exhibits an ionic radii difference of 0.135 Å between high-spin Fe^{2+} ($r = 0.78$ Å) and Fe^{3+} ($r = 0.645$ Å).[32]

Futhermore, it was recently reported that for $LiFe_2O_4$, phase separation can be inhibited in small crystal particles or at high charge–discharge rates.[37,38] However, the present model states that phase separation is an iherent feature in battery materials with large lattice changes without diffusion limitation and cannot be influenced by these two paramters. Evidence for this claim is that, all of the $Ni(OH)_2$ materials reported so far in the literature, irrespective of their particle size and morpology or the charge–discharge rate, exhibit the similar charge–discharge hysteresis shown above. For example, recently nanosheets and even monolayers of $Ni(OH)_2$ were reported, but they also exhibit the typical CV hysteresis of $Ni(OH)_2$.[39,40]

Finally, the effect of interfacial and solid ion diffusion on the insertion electrochemistry was not treated here. Generally, diffusion influences insertion reactions at high electrode thicknesses (or large particle sizes) and high charge–discharge rates.[41–44] In other words, when ion diffusion takes longer than the time of experiment, the overall reaction is controlled by diffusion; otherwise, the insertion reaction is surface-controlled (or reaction-driven) as in the present study. Very recently, Fraggedakis et al. showed for the phase-separating Li_xC_6 single particles that under diffusion control, the intercalation proceeds through a shrinking-core mode with axisymmetric profiles, but under quasi-equilibrium reaction-driven condition, intercalaction proceeds in a frontal mode (intercalation wave)[45] as in the present study. Nontheless, the effect of diffusion on the intercalation pathways and its implications requires further investigation.

Table 1. Effective ionic radii of nickel and cobalt ions in two different oxidation states with octahedral coordination (LS and HS stand for low-spin and high-spin, respectively).[32]

Ion	Radius (r, [Å])	Δr [Å]
Co^{3+}	0.54^{LS}	
Co^{4+}	0.53^{HS}	0.01
Ni^{2+}	0.69	
Ni^{3+}	0.56^{LS}	0.13

Conclusion

Battery characterization with simple methods is very essential for the development of batteries. Here, a thermodynamic model is developed to study and even predict the hysteresis of ion insertion/expulsion battery materials based on cyclic voltammetry. The model was experimentally verified for $Ni(OH)_2$ and CoOOH cathodes. The origin of charge–discharge hysteresis in

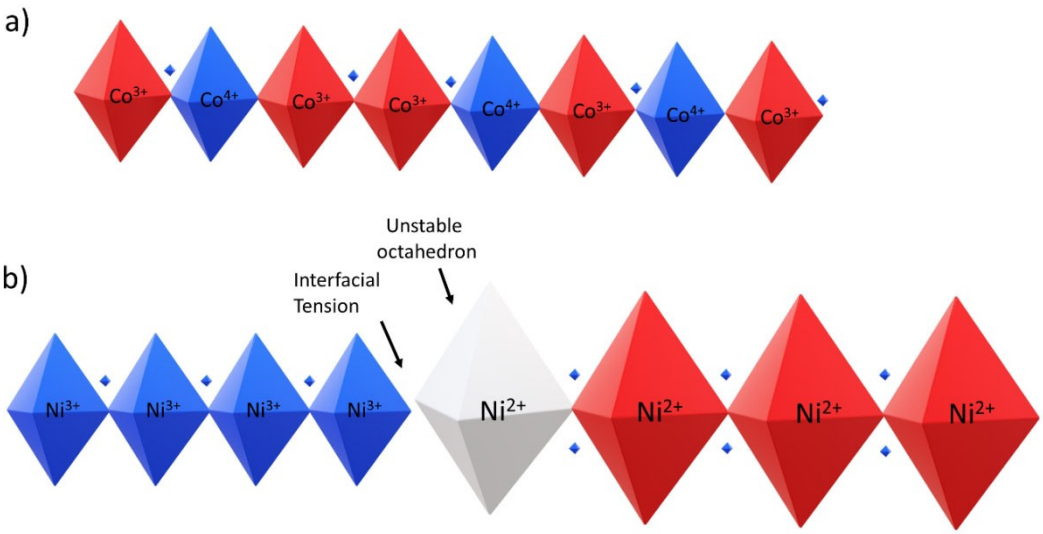

Scheme 2. A cross-sectional view of a crystal layer of CoOOH (a) and $Ni(OH)_2$ (b) during oxidation. The blue balls exhibit hydrogen atoms. (Oxygen atoms, which are located at the corners of octahedra, and polyhedral distortions are not shown for simplicity of presentation).

these materials was related to phase separation and inability to re-establish the same reaction path during backward reaction. It was revealed that CoOOH forms nearly a solid solution, but $Ni(OH)_2$ undergoes a phase separation during charge–discharge. The extent of charge–discharge hysteresis in these materials was expressed with an interfacial Gibbs energy based on an interfacial tension parameter and a path symmetry factor. Furthermore, a microscopic view indicates that phase separation and reaction path dissymmetry are a result of large ionic radii changes in the central metal atoms before and after oxidation.

Finally, the present model has two important implications for batteries:

I. The extent of phase separation and hysteresis in battery electrodes can be predicted based on the Δr parameter that establishes a criterion of ideally $\Delta r = 0$ for a solid solution behavior.
II. When batteries undergo phase separation during charge and discharge, the dissimilar interfacial energies result in a low energy efficiency, and their exponential increase cause the reaction front to stop at some point, leading to a capacity much lower than the theoretical one.

Experimental

Materials and methods

The chemicals $Ni(NO_3)_2 \cdot 6H_2O$, $Co(NO_3)_2 \cdot 6H_2O$, KOH, and KCl were purchased from Sigma–Aldrich Company and used as received. Lab-customized Pt rods (~0.38 mm diameter and 0.29-36 cm^{-2} area) were used as current collector for the electrochemical deposition of the samples. For the theoretical section, a Python IDE was used to plot $E(x)$ and $I(x)$ functions against each other in the range $0 < x < 1$.

Electrode preparation

In order to prepare ion-insertion electrodes that are free from diffusion effects, thin films of metal hydroxides were electrodeposited on Pt rods as follows:

$Ni(OH)_2$ electrode:. First, the Pt rods were cleansed carefully in aqua regia for 5 to 10 minutes and washed with deionized water (DI). The electrodeposition was conducted in the potentiostatic mode, i.e., chronoamperometry, at room temperature (25.0 °C) on the Pt rods from aqueous solution of 10 mM $Ni(NO_3)_2 \cdot 6H_2O$ with a deposition potential of −0.85 V (vs. Ag/AgCl) for 1 minutes. After deposition, the electrode was cleansed with DI water and left to dry at room temperature for about 30 minutes.

CoOOH electrode: CoOOH electrodes were prepared in two steps. First, $Co(OH)_2$ is deposited by a similar procedure as above from an aqueous solution of 0.1 M $Co(NO_3)_2$ for 5 s. Then, a cyclic voltammogram is carried out between −0.05 V and 0.35 V in a solution of 0.1 M KOH at a scan rate of 5 $mV\,s^{-1}$ to irreversibly oxidize $Co(OH)_2$ to CoOOH.[46]

Electrochemical measurements

The electrochemical measurements were carried out in a three-electrode configuration in aqueous solution using cyclic voltammetry (CV) on an Autolab (PGSTAT12) instrument. The as-prepared electrodes, a Pt coil, and an Ag/AgCl (saturated KCl) electrode were used as working, counter, and reference electrodes, respectively. A salt bridge consisted of Agar and saturated KNO_3 is used to avoid chloride leakage and also to reduce the junction potential. The potential of the reference electrode is 197.0 mV vs. standard hydrogen electrode (SHE). All electrochemical measurements were carried out at 25 °C which is also assumed in the theoretical section.

The cyclic voltammograms (CV) were recorded in 0.1 M KOH (pH = 12.8) and each CV repeated at least 5 times with different electrodes to ensure the reproducibility of the CV curves and the current-scan rate relationships.

Acknowledgements

The authors would like to thank the Alexander von Humboldt Foundation for supporting this work under a postdoctoral research fellowship. Open Access funding enabled and organized by Projekt DEAL.

Conflict of Interest

There are no conflicts to declare.

Data Availability Statement

The data that support the findings of this study are available from the corresponding author upon reasonable request.

Keywords: Cobalt · Hysteresis · Ion insertion · Nickel · Phase transition

[1] A. Laurita, L. Zhu, P.-E. Cabelguen, J. Auvergniot, J. Hamon, D. Guyomard, N. Dupré, P. Moreau, *ACS Appl. Mater. Interfaces* **2022**, *14*, 41945–41956.
[2] L. De Biasi, A. O. Kondrakov, H. Geßwein, T. Brezesinski, P. Hartmann, J. Janek, *J. Phys. Chem. C* **2017**, *121*, 26163–26171.
[3] K. P. Ta, J. Newman, *J. Electrochem. Soc.* **1998**, *145*, 3860–3874.
[4] V. Srinivasan, J. W. Weidner, J. Newman, *J. Electrochem. Soc.* **2001**, *148*, A969–A980.
[5] K. P. Ta, J. Newman, *J. Electrochem. Soc.* **1999**, *146*, 2769–2779.
[6] A. Van der Ven, K. A. See, L. Pilon, *Batter. Energy* **2022**, *1*, 20210017.
[7] D. A. Kitchaev, J. Vinckeviciute, A. Van Der Ven, *J. Am. Chem. Soc.* **2021**, *143*, 1908–1916.
[8] B. Lu, Y. Song, Q. Zhang, J. Pan, Y. T. Cheng, J. Zhang, *Phys. Chem. Chem. Phys.* **2016**, *18*, 4721–4727.
[9] J. Lim, Y. Li, D. H. Alsem, H. So, S. C. Lee, P. Bai, D. A. Cogswell, X. Liu, N. Jin, Y. S. Yu, N. J. Salmon, D. A. Shapiro, M. Z. Bazant, T. Tyliszczak, W. C. Chueh, *Science* **2016**, *353*, 566–571.
[10] W. Dreyer, J. Jamnik, C. Guhlke, R. Huth, J. Moškon, M. Gaberšček, *Nat. Mater.* **2010**, *9*, 448–453.
[11] H. D. Deng, H. Zhao, N. Jin, L. Hughes, B. H. Savitzky, C. Ophus, D. Fraggedakis, A. Borbély, Y. S. Yu, E. G. Lomeli, R. Yan, J. Liu, D. A. Shapiro, W. Cai, M. Z. Bazant, A. M. Minor, W. C. Chueh, *Nat. Mater.* **2022**, *21*, 547–554.
[12] P. G. Bruce, Ed., *Solid State Electrochemistry*, Cambridge University Press, Cambridge, **1995**.
[13] P. J. Gellings, H. J. M. Bouwmeester, *The CRC Handbook of Solid State Electrochemistry*, CRC Press, Boca Raton FL, **1997**.

[14] H. Chen, E. Kätelhön, R. G. Compton, *J. Phys. Chem. Lett.* **2022**, *13*, 536–543.
[15] A. Doménech-Carbó, *J. Phys. Chem. C* **2022**, *126*, 11822–11832.
[16] J. C. Myland, K. B. Oldham, *Electrochem. Commun.* **2005**, *7*, 282–287.
[17] J. Waelder, R. Vasquez, Y. Liu, S. Maldonado, *J. Am. Chem. Soc.* **2022**, *144*, 6410–6419.
[18] J. Waelder, S. Maldonado, *Anal. Chem.* **2021**, *93*, 12672–12681.
[19] Y. B. Vogel, A. Molina, J. Gonzalez, S. Ciampi, *Anal. Chem.* **2019**, *91*, 5929–5937.
[20] E. Laviron, *J. Electroanal. Chem.* **1979**, *100*, 263–270.
[21] N. Eliaz, E. Gileadi, *Physical Electrochemistry Fundamentals Techniques and Applications*, Wiley-VCH, Weinheim, **2019**.
[22] M. D. Levi, D. Aurbach, *Electrochim. Acta* **1999**, *45*, 167–185.
[23] E. M. Gavilán-Arriazu, D. E. Barraco, E. P. M. Leiva, *J. Solid State Electrochem.* **2021**, *25*, 2793–2806.
[24] F. Scholz, M. Lovrić, Z. Stojek, *J. Solid State Electrochem.* **1997**, *1*, 134–142.
[25] V. Srinivasan, J. W. Weidner, R. E. White, *J. Solid State Electrochem.* **2000**, *4*, 367–382.
[26] B. E. Conway, *Electrochemical Supercapacitors Scientific Fundamentals and Technological Applications*, Kluwer Acad. [U.A.], New York, **1999**.
[27] D. S. Hall, D. J. Lockwood, C. Bock, B. R. MacDougall, *Proc. R. Soc. A Math. Phys. Eng. Sci.* **2015**, *471*, 20140792.
[28] B. Ash, V. S. Nalajala, A. K. Popuri, T. Subbaiah, M. Minakshi, *Nanomaterials* **2020**, *10*, 1–22.
[29] Q. Hu, Y. Xue, J. Kang, I. Scivetti, G. Teobaldi, A. Selloni, L. Guo, L. M. Liu, *ACS Catal.* **2022**, *12*, 295–304.
[30] A. O. Kondrakov, A. Schmidt, J. Xu, H. Geßwein, R. Mönig, P. Hartmann, H. Sommer, T. Brezesinski, J. Janek, *J. Phys. Chem. C* **2017**, *121*, 3286–3294.
[31] A. O. Kondrakov, H. Geßwein, K. Galdina, L. De Biasi, V. Meded, E. O. Filatova, G. Schumacher, W. Wenzel, P. Hartmann, T. Brezesinski, J. Janek, *J. Phys. Chem. C* **2017**, *121*, 24381–24388.
[32] R. D. Shannon, *Acta Crystallogr.* **1976**, *A32*, 751–767.
[33] A. Bergmann, T. E. Jones, E. Martinez Moreno, D. Teschner, P. Chernev, M. Gliech, T. Reier, H. Dau, P. Strasser, *Nat. Catal.* **2018**, *1*, 711–719.
[34] M. Bajdich, M. García-Mota, A. Vojvodic, J. K. Nørskov, A. T. Bell, *J. Am. Chem. Soc.* **2013**, *135*, 13521–13530.
[35] A. Moysiadou, S. Lee, C. S. Hsu, H. M. Chen, X. Hu, *J. Am. Chem. Soc.* **2020**, *142*, 11901–11914.
[36] A. J. Tkalych, K. Yu, E. A. Carter, *J. Phys. Chem. C* **2015**, *119*, 24315–24322.
[37] A. Sood, A. D. Poletayev, D. A. Cogswell, P. M. Csernica, J. T. Mefford, D. Fraggedakis, M. F. Toney, A. M. Lindenberg, M. Z. Bazant, W. C. Chueh, *Nat. Rev. Mater.* **2021**, *6*, 847–867.
[38] P. Bai, D. A. Cogswell, M. Z. Bazant, *Nano Lett.* **2011**, *11*, 4890–4896.
[39] A. Harvey, X. He, I. J. Godwin, C. Backes, D. McAteer, N. C. Berner, N. McEvoy, A. Ferguson, A. Shmeliov, M. E. G. Lyons, V. Nicolosi, G. S. Duesberg, J. F. Donegan, J. N. Coleman, *J. Mater. Chem. A* **2016**, *4*, 11046–11059.
[40] J. Kang, Y. Xue, J. Yang, Q. Hu, Q. Zhang, L. Gu, A. Selloni, L. M. Liu, L. Guo, *J. Am. Chem. Soc.* **2022**, *144*, 8969–8976.
[41] E. M. Gavilán-Arriazu, D. E. Barraco, Y. Ein-Eli, E. P. M. Leiva, *J. Solid State Electrochem.* **2022**, *26*, 1995–2003.
[42] M. D. Levi, D. Aurbach, *J. Solid State Electrochem.* **2007**, *11*, 1031–1042.
[43] M. D. Levi, D. Aurbach, *J. Solid State Electrochem.* **2008**, *12*, 409–420.
[44] E. M. Gavilán-Arriazu, D. E. Barraco, Y. Ein-Eli, E. P. M. Leiva, *ChemPhysChem* **2022**, *202200665*, DOI 10.1002/cphc.202200665.
[45] D. Fraggedakis, N. Nadkarni, T. Gao, T. Zhou, Y. Zhang, Y. Han, R. M. Stephens, Y. Shao-Horn, M. Z. Bazant, *Energy Environ. Sci.* **2020**, *13*, 2142–2152.
[46] J. A. Koza, C. M. Hull, Y. C. Liu, J. A. Switzer, *Chem. Mater.* **2013**, *25*, 1922–1926.

Manuscript received: November 29, 2022
Revised manuscript received: January 11, 2023
Version of record online: January 23, 2023